Surface Science 622 (2014) 35–43

Contents lists available at ScienceDirect

Surface Science

journal homepage: www.elsevier.com/locate/susc

The structural analysis of Cu(111)-Te $\left(\sqrt{3}\times\sqrt{3}\right)$R30° and $\left(2\sqrt{3}\times2\sqrt{3}\right)$R30° surface phases by quantitative LEED and DFT

M. Lahti [a], A. Chaudhuri [a], K. Pussi [a,*], D. Hesp [b,c], I.M. McLeod [b,c], V.R. Dhanak [b,c], M.O. King [d,e], M. Kadodwala [d], D.A. MacLaren [e]

[a] Lappeenranta University of Technology, Department of Physics and Mathematics, P.O. Box 20, FIN-53051 Lappeenranta, Finland
[b] Department of Physics, University of Liverpool, Liverpool L69 3BX, UK
[c] The Stephenson Institute for Renewable Energy, University of Liverpool, Liverpool L69 3BX, UK
[d] School of Chemistry, University of Glasgow, Glasgow G12 8QQ, UK
[e] SUPA, School of Physics and Astronomy, University of Glasgow, Glasgow G12 8QQ, UK

ARTICLE INFO

Article history:
Received 12 September 2013
Accepted 17 November 2013
Available online 17 December 2013

Keywords:
Low energy electron diffraction (LEED)
Density functional theory (DFT)
Copper telluride

ABSTRACT

The chemisorption of tellurium on atomically clean Cu(111) surface has been studied under ultra-high vacuum conditions. At room temperature, the initial stage of growth was an ordered $\left(2\sqrt{3}\times2\sqrt{3}\right)$R30° phase (0.08 ML). An ordered $\left(\sqrt{3}\times\sqrt{3}\right)$R30° phase is formed at 0.33 ML coverage of Te. The adsorption sites of the Te atoms on the Cu(111) surface at 0.08 ML and 0.33 ML coverages are explored by quantitative low energy electron diffraction (LEED) and density functional theory (DFT). Our results indicate that substitutional surface alloy formation starts at very low coverages.

1. Introduction

After decades of research, the adsorption of Te on copper remains interesting because of its technological importance. A crucial component of a solar cell is its back contact which is typically made of CuTe [1]. The efficiency of a solar cell can be increased through the back-contact, by controlling the doping amount of Te into Cu. In addition to the application in solar cell industry, the complexity and the richness of the alloy phases of this material [2,3] and the ability to tune the electronic properties by altering relative composition, makes CuTe attractive for scientific research.

Even though a number of studies have been done on polycrystalline copper telluride system [4–8], studies on the gas phase deposition of Te on a low index, single Cu(111) crystal are limited. An early, off normal, low energy electron diffraction study [9] mentioned the formation of well ordered $\left(2\sqrt{3}\times2\sqrt{3}\right)$R30° phase at the very low coverage of Te (0.08 ML). According to this experiment, the Te atoms chemisorped on the underlying Cu(111) surface, occupying a single bridge position, between two below-lying Cu atoms. In contrast, later, the result from a SEXAFS study [10] on this system, indicated the possibility of surface substitutional alloy formation.

A recent, more detailed characterization of growth of Te on Cu(111) surface [11] by vapor deposition, confirmed the appearance of the $\left(2\sqrt{3}\times2\sqrt{3}\right)$R30° LEED spots at ~0.08 ML. The spots were reported to be sharpest around 0.17 ML coverage of Te. After that, the LEED spots progressively became diffuse with an increase of Te coverage up to 0.3 ML. The combined STM, XPS and UPS studies on this phase concluded the direct incorporation of the Te atoms in the surface plane of Cu(111) which supported the surface alloying suggested earlier [10]. A $\left(\sqrt{3}\times\sqrt{3}\right)$R30° LEED structure was observed with further deposition of Te up to 0.68 ML, at room temperature. Initially, this phase remained disordered. The LEED spots became sharp after annealing at about 300 °C for 5 min, at a Te coverage around 0.25 ML. Similar to the low coverage $\left(2\sqrt{3}\times2\sqrt{3}\right)$ phase, the results from STM and XPS studies indicate the surface substitutional surface alloy formation for the $\left(\sqrt{3}\times\sqrt{3}\right)$R30° structure. However, the alloying was restricted to the uppermost (111) layer. At high coverage, >0.69 ML of Te, the $\left(\sqrt{3}\times\sqrt{3}\right)$R30° pattern retained its symmetry but STM measurement revealed a ~3.2% in plane lattice contraction with respect to the lower coverage structures. The binding energies of the Cu 2p and Te 3d spectra, attributed to the surface substitutional alloy phase in case of $\left(\sqrt{3}\times\sqrt{3}\right)$R30° were absent. Thus, based on the observation of both the XPS and STM experiments, a complete formation of an ordered Cu_3Te_2-like alloy phase was proposed.

Tellurium atomic layers, formed by evaporative deposition in vacuum, on other fcc(111) metal surfaces have been studied by a variety of different surface sensitive techniques. LEED studies of Te on Ni(111)

* Corresponding author.
E-mail address: katariina.pussi@lut.fi (K. Pussi).

0039-6028/$ – see front matter © 2013 Elsevier B.V. All rights reserved.
http://dx.doi.org/10.1016/j.susc.2013.11.018

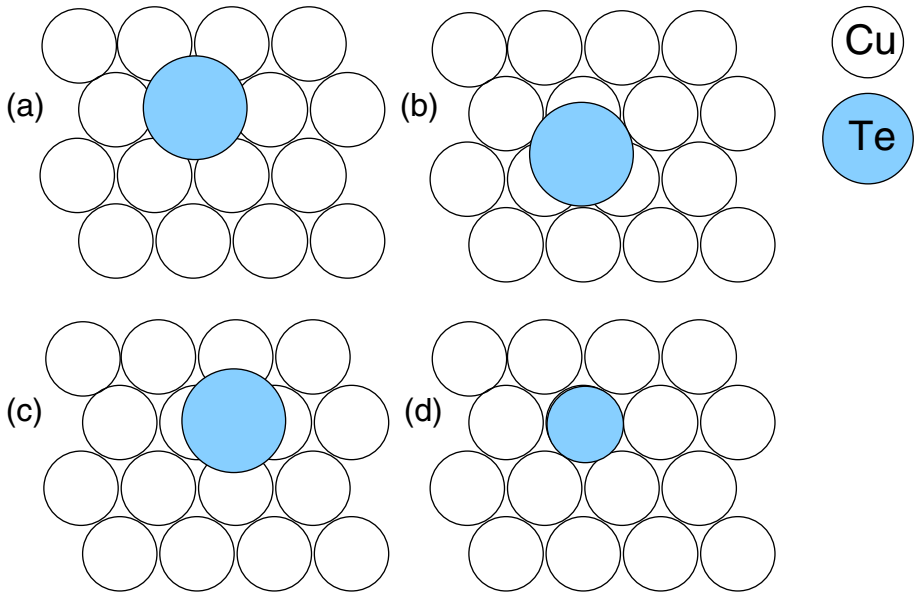

Fig. 1. Top views of the adsorption sites used in LEED and DFT analysis. (a) Top site. (b) Hollow site. In hcp hollow there is an atom in the second substrate layer just below the adsorbate and in fcc hollow the next atom below the adsorbate is in the third substrate layer. (c) Bridge site. (d) Surface alloy. Only the top layer copper atoms are shown.

reported a $\left(2\sqrt{3}\times 2\sqrt{3}\right)$R30°, $\left(\sqrt{3}\times\sqrt{3}\right)$R30°, and complex patterns [12,13]. Angular resolved photoemission studies of the Ni(111)-$\left(\sqrt{3}\times\sqrt{3}\right)$R30° suggested that Te atoms in this structure are bound in threefold hollow sites [14–16]. On Au(111) LEED results show that the first monolayer of Te is arranged with an incommensurate Au(111)-$\left(\sqrt{3}\times\sqrt{3}\right)$R30°-Te structure, and after the completion of the first monolayer, a (3×3)-Te structure appears [17]. In $\left(\sqrt{3}\times\sqrt{3}\right)$R30° phase the adatoms are believed to occupy the three-fold hollow sites of the underlying Au(111) substrates [18].

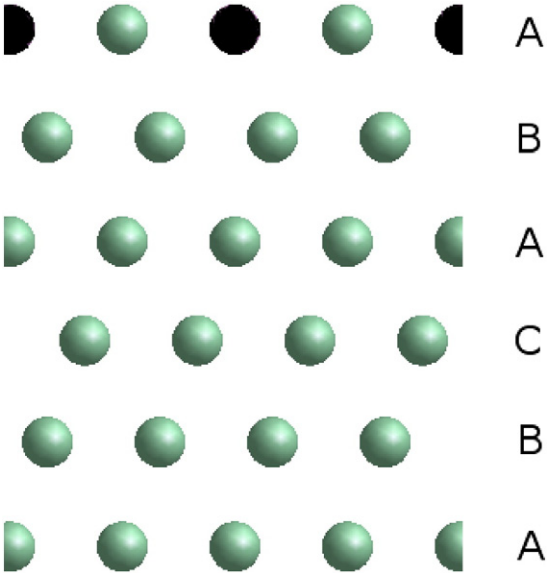

Fig. 2. Side view for the faulted alloy structure for $\left(\sqrt{3}\times\sqrt{3}\right)$R30° phase. The capital letters represent the ABC-stacking for fcc(111) surface. Black atoms are tellurium and green atoms are copper.

Antimony, which is next to the tellurium in the periodic table, has been studied on Ag(111) and Cu(111) surfaces [19]. For both substrates at coverages below 0.33 ML, the Sb atoms are embedded randomly into the surface layer, forming a substitutional surface alloy. A sudden formation of $\left(\sqrt{3}\times\sqrt{3}\right)$R30° stacking fault alloy is reported when the coverage becomes near 0.33 ML [19]. Medium energy ion scattering measurements performed on Cu(111)-$\left(\sqrt{3}\times\sqrt{3}\right)$R30°-Sb [20] are found to be consistent with the stacking fault position proposed by de Vries et al. [19]. The driving force for this reconstruction is proposed to be the repulsive interaction between Sb atoms [19].

In this paper we present a detailed analysis of the structures of the 0.08 ML and 0.33 ML phases of Te on Cu(111) surface by quantitative LEED and DFT.

2. Experiment

The experiments were carried out in a standard ultra high vacuum (UHV) chamber equipped with a rear-view LEED optics from OCI Vacuum Microengineering and an electron energy analyzer with dual anode X-ray source from PSP Vacuum Technology. The chamber has been

Table 1
Pendry *R*-factors for different structures for $\left(2\sqrt{3}\times 2\sqrt{3}\right)$-phase and $\left(\sqrt{3}\times\sqrt{3}\right)$ phase. The last line shows the Pendry variance. The values with bold font are the values that fit inside the Pendry variance and thus are possible structures.

Geometry	Pendry *R*-factor $\left(2\sqrt{3}\times 2\sqrt{3}\right)$	Pendry *R*-factor $\left(\sqrt{3}\times\sqrt{3}\right)$
Top	0.26	0.70
Fcc hollow	0.29	0.67
Hcp hollow	**0.22**	**0.36**
Bridge	0.59	0.54
Alloy	**0.24**	0.54
Faulted alloy	0.48	**0.41**
Variance	0.03	0.06

Table 2
Some of the optimized structural parameters from the LEED analysis for the best fit geometries for both coverages.

Geometry	d(Te–Cu)	dz_{Te-Cu^1}	$dz_{Cu^1-Cu^2}$	$dz_{Cu^2-Cu^3}$	$dz_{Cu^3-Cu^4}$
$2\sqrt{3} \times 2\sqrt{3}$					
Hcp hollow	2.76 ± 0.02 Å	2.33 ± 0.02 Å	2.06 ± 0.03 Å	2.06 ± 0.04 Å	
Alloy	2.71 ± 0.03 Å	0.91 ± 0.03 Å	2.08 ± 0.04 Å	2.00 ± 0.04 Å	
$\sqrt{3} \times \sqrt{3}$					
Hcp hollow	2.74 ± 0.04 Å	2.31 ± 0.04 Å	2.06 ± 0.04 Å	2.04 ± 0.07 Å	2.09 ± 0.10 Å
Faulted alloy	2.70 ± 0.05 Å	0.88 ± 0.05 Å	2.12 ± 0.06 Å	2.03 ± 0.07 Å	2.060.09 Å

described in detail elsewhere [11]. The base pressure of the chamber was 2×10^{-10} mbar. The Cu(111) crystal sample was cleaned insitu by usual combination of Ar ion bombardment (1 kV, 8 μA) and annealing (approximately 830 K) cycles. The crystal order and cleanliness were checked by LEED and XPS. When sharp (1×1) integral ordered LEED spots were observed and no traces of contamination were found in XPS spectra, the surface was considered as well-ordered and clean. Te was deposited from a homemade Knudsen effusion cell held at 570 K. The deposition rate for the submonolayer coverage was calculated to be ~0.2 ML/min measuring Cu $2p_{3/2}$ and Te $3d_{5/2}$ XPS spectra and known cross-section [21–23]. The substrate was kept at room temperature (300 K), during the surface preparation. Once the superstructures were observed by LEED, the sample was annealed to a higher temperature and then cooled down to 140 K for the LEED intensity measurement. Cooling enhanced the contrast and sharpened the LEED spots. The intensities of the diffracted spots were acquired with a CCD camera interfaced to PC. The intensities of the beams were collected at normal incidence as a function of the energy of the incident electrons (LEED $I(E)$ spectra). The spectra were background subtracted and normalized with respect to the primary beam current. The intensities of the symmetrically equivalent spots were averaged to reduce the experimental noise.

3. Calculations

3.1. LEED

The theoretical LEED $I(E)$ curves were calculated using the Barbieri/Van Hove Symmetrized Automated Tensor LEED package [24]. The phase shifts were calculated with the Barbieri/Vanhove phase shift package [24]. Twelve phase shifts were used to describe the scattering. The imaginary part of the inner potential was set to −5 eV and the real part of the inner potential was assumed to be energy independent and allowed to vary to obtain the optimal value. The Debye temperatures used for Cu and Te were 343 K and 153 K at the initial stage of calculation and these numbers were optimized later. The agreement between the calculated and experimental $I(E)$ curves was quantified with Pendry reliability factor and the error bars for the determined parameters were calculated using Pendry RR-function [25]. The trial structures were optimized by varying the position of the adsorbed Te atoms and the first three to five substrate Cu layers. The number of optimized parameters was chosen so that both the length of the data set and the size of the unit cell were taken into account. Three fold rotational symmetry with a mirror plane was assumed during the structural optimization of the clean copper surface and all the trial structures except the bridge site. For the bridge site, the proper symmetry was restored by domain averaging.

3.2. DFT

The static calculations for total energies were performed using the Vienna ab-initio simulation package (VASP) [26–30] including the projector augmented wave (PAW) [31] potentials. A kinetic energy cut-off of 500 eV was applied for the plane waves. The exchange and correlation functional were treated by the generalized-gradient approximation (GGA) of Perdew–Burke–Ernzerhof (PBE) [32]. The $10 \times 8 \times 1$ Monkhorst–Pack mesh [33] was used for k-point sampling. The Cu surface was modeled using the supercell approach, where periodic boundary conditions are applied to the central supercell so that it is reproduced periodically throughout xy-space. The surface slab was modeled with 6 layers of Cu atoms. A region of approximately 10 Å of

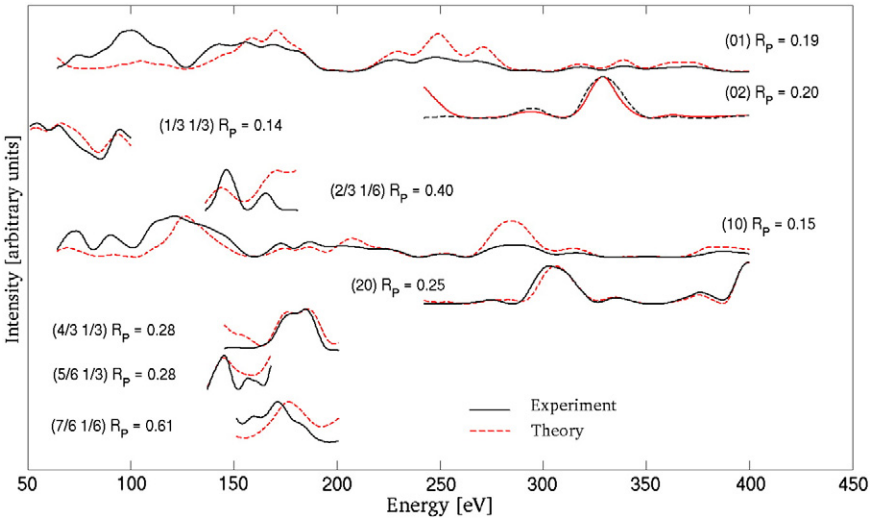

Fig. 3. The best fit $I(E)$ curves for the $\left(2\sqrt{3} \times 2\sqrt{3}\right)$R30° phase (hcp hollow). Pendry R-factors for each beam are shown. The overall Pendry R-factor is 0.22.

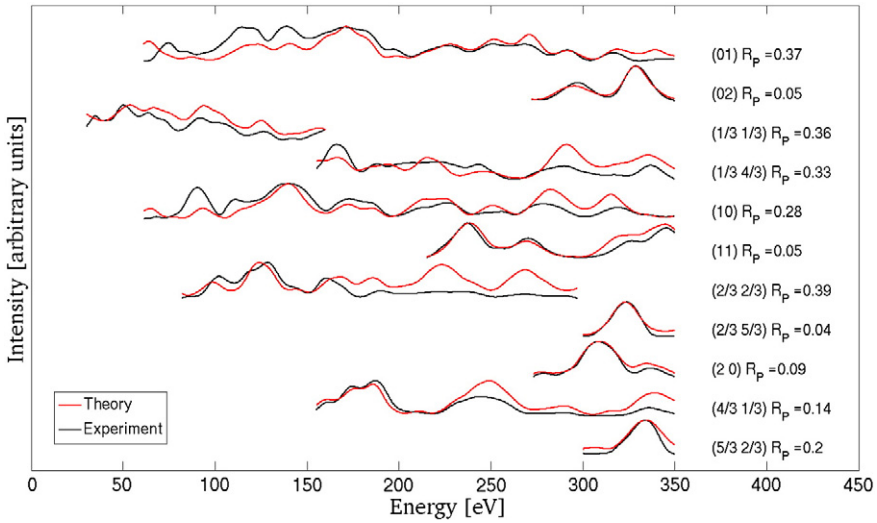

Fig. 4. The best fit $I(E)$ curves for the $\left(\sqrt{3}\times\sqrt{3}\right)$R30° phase (40:60 mix of hcp hollow and fauted alloy). Pendry R-factors for each beam are shown. The overall Pendry R-factor is 0.26.

vacuum was inserted in the z-direction to prevent interactions occurring between mirror images. The bottommost layer of the surface slab was frozen during the geometry relaxation. The simulated STM images were calculated using p4VASP [34].

The adsorption energies of a Te atom are defined as:

$$E_{ads} = \frac{1}{N_{Te}}(E_{tot} - E_{clean} - N_{Te}E_{Te})$$

where E_{tot} is total energy of a relaxed Cu/Te supercell; E_{clean} is the total energy of the relaxed clean Cu slab; N_{te} is the number of Te atoms and E_{Te} is the energy of one atom in the bulk of Te metal. For substitutional alloy structures the adsorption energy is defined as:

$$E_{ads} = \frac{1}{N_{Te}}(E_{tot} - E_{clean} - N_{Te}E_{Te} + N_{Te}E_{Cu\text{-}bulk})$$

where $E_{Cu\text{-}bulk}$ is the total energy of a Cu bulk atom.

4. Results

4.1. LEED

In order to validate the quality of our copper sample, intensities of five non-equivalent beams were collected at 300 K from the clean Cu(111) surface and a dynamical LEED calculation was done. This led to a good agreement between theoretical and experimental $I(E)$ curves, with R_P of 0.14. The interlayer spacings of the first three layers were found to remain essentially the same as the bulk value, which is in agreement with the earlier work done on this surface [35].

Table 3
DFT adsorption energies for different structures for $\left(2\sqrt{3}\times 2\sqrt{3}\right)$-phase and $\left(\sqrt{3}\times\sqrt{3}\right)$ phase.

Geometry	Adsorption energy [eV] $\left(2\sqrt{3}\times 2\sqrt{3}\right)$	Adsorption energy [eV] $\left(\sqrt{3}\times\sqrt{3}\right)$
Top	–	−0.93
Fcc hollow	−1.53	−1.23
Hcp hollow	−1.50	−1.23
Bridge	−1.46	−1.26
Alloy	−1.60	−1.39
Faulted alloy	−1.50	−1.29

4.1.1. $\left(2\sqrt{3}\times 2\sqrt{3}\right)R30°$ phase

The first ordered phase observed during Te deposition on Cu(111) surface, was reported to be the $\left(2\sqrt{3}\times 2\sqrt{3}\right)$R30° structure [9,11] at very low coverage (0.08 ML). Total of nine beams, out of which four were for integral and five for fractional order spots, were collected to evaluate this structure. Electron energies were ranging from 60 eV to 400 eV with a cumulative energy of 1250 eV. Six different trial structures were tested. The Te atoms were placed on top, bridge and three-fold fcc or hcp hollow sites on the flat (111) Cu surface (Fig. 1) to construct four high symmetry models. For the remaining two trial structures, two surface substitutional alloy models were constructed. In the first alloy model one Cu atom in the surface layer was replaced with a Te atom, so that one Te atom and 11 Cu atoms remained in the unit cell at the first layer. The second alloy model (faulted alloy) has similarly one Te atom substituted into the first copper layer and in addition to this a stacking fault is introduced to the surface, so that the top layer atoms are sitting at hcp hollows and not in fcc hollows as they would if the stacking was perfect fcc(111)-type. Fig. 2 describes the faulted alloy structure. This structural model was previously observed for Sb on the Cu(111) surface [20].

The start geometry for each structure optimization was a bulk terminated Cu(111) surface with the Te atoms at the respective adsorption positions considering the hard sphere model with a Cu of radius 1.28 Å and Te of radius 1.43 Å. The Te atoms and the first three Cu layers are allowed to relax in the vertical direction for the LEED analysis. At the first stage, the Te atoms along with the 1st layer of Cu atoms, were allowed to relax. Once the referred co-ordinates were optimized, successively, the second and the third layers of substrate Cu atoms were included for vertical relaxation. Three different sets of phase shifts, one for Te, one for surface Cu layers and one for bulk Cu, were used. The non-structural parameters, i.e., the imaginary part of the inner potential, l_{max} and Debye temperature were optimized in the final stage of the calculation.

The data set used is dominated by the integer order beams. Out of the 1250 eV cumulative energy range only 250 eV is from fractional order beams. Braun and Held have demonstrated that the information contained in the IV-curves of integer-order spots is sufficient for an accurate structure determination [37]. However, the limited length of our data set decreases the R-factor contrast between different adsorption sites. The agreements of the $I(E)$ curves for fractional order spots, which are considered to be dominated by the absorption sites, favor the hcp ($R_P = 0.22$) and alloy ($R_P = 0.24$) structures. The Pendry

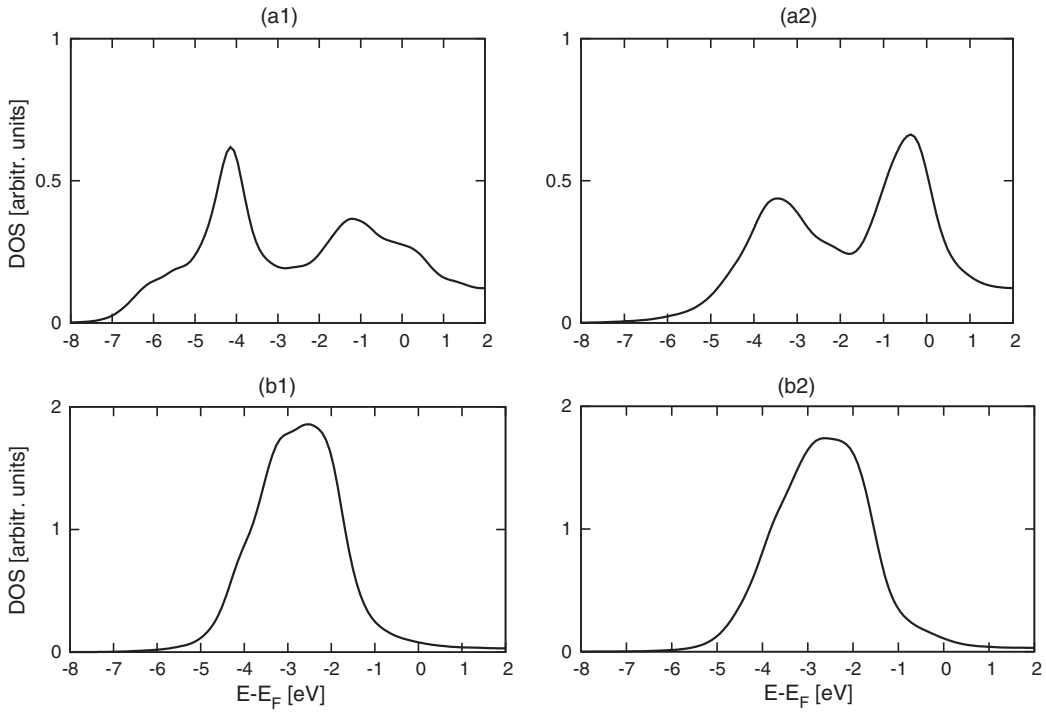

Fig. 5. The Local DOS of the surface atoms of the $\left(\sqrt{3}\times\sqrt{3}\right)$R30° phase. (a1) The p-DOS of Te at the surface alloy. (a2) the p-DOS of Te at the hcp site. (b1) The d-DOS of the Cu atom next to the surface alloy Te. (b2) The d-DOS of the Cu atom next to the Te on the hcp site.

variance of 0.03 was calculated with the help of the Pendry RR function [25], which allows us to rule out other geometries except the hcp hollow and alloy.

The Cu–Te bond length for hcp-hollow structure is 2.76 Å and for the alloy 2.71 Å. These numbers are slightly longer than the value reported in the earlier work [9] and the bond length in Cu_2Te structure (2.67 Å) [36]. The Pendry *R*-factors are listed in Table 1 and some of the optimized geometrical parameters for the best fit structure are listed in Table 2. The possibility of mixed surface geometry was tested by incoherent mixing of alloy with hcp structure. This improved the agreement only slightly; 50:50 mix giving Pendry *R*-factor of 0.21. The experimental and calculated $I(E)$ curves for the hcp hollow structure are shown in Fig. 3.

General level of agreement reached in the quantitative LEED analysis for the 0.08 ML coverage is good. However, since the majority of the cumulative data range is of integer order spots, this could be expected. It is common experience from LEED-IV analysis that better agreement can be achieved for the IV-curves of the integer-order spots. These carry large contributions from diffraction by the bulk-like layers below the surface region where the structure is known and is better described by the muffin-tin potentials used in standard LEED theory [37].

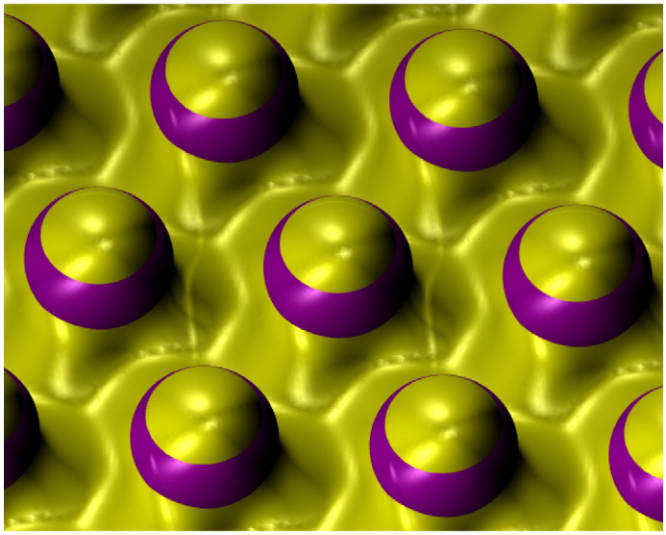

Fig. 6. 3-Dimensional plot of the partial charge density Te/Cu surface in the case of Te on the hcp-hollow site with the coverage 0.33 ML. The colors in the figure represent the following energy values: yellow: −6…−2 eV below Fermi level, purple: −1.8…0 eV below Fermi level.

4.1.2. $\left(\sqrt{3}\times\sqrt{3}\right)R30°$ phase

In order to evaluate the $\left(\sqrt{3}\times\sqrt{3}\right)$R30° surface phase, the LEED $I(E)$ data was recorded with electron energies between 30 eV to 350 eV. The data set consists of five integer order and six fractional order beams, with a cumulative energy of 1675 eV. The Te density that corresponds to the structure $\left(\sqrt{3}\times\sqrt{3}\right)$R30° is consistent with one Te atom per unit cell. The same six different model structures as in the low coverage case were tested.

The start geometries of each model were again calculated considering the hard sphere of Cu and Te radii, mentioned in earlier section. Three different sets of phase shifts, one for Te, one for surface Cu layers and one for bulk Cu, were used. Te atoms and first five layers of Cu were allowed to relax perpendicular to the surface in the initial stage for the coordinate search. The non structural parameters were optimized at the final stage of analysis. Table 1 shows the R_P values, obtained from the analysis and some of the optimized geometrical parameters for the best fit structure are listed in Table 2. The R_P values are a bit lower for the hcp and the faulted alloy structures compared to the other trial

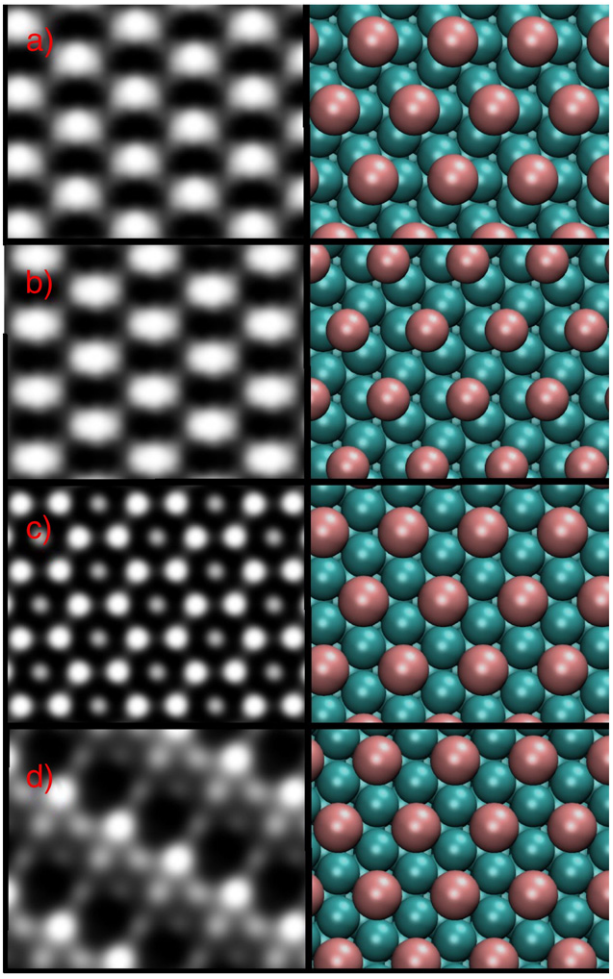

Fig. 7. Simulated STM images along with the top view of the structure for the hollow and alloy adsorption geometries in the $\left(\sqrt{3}\times\sqrt{3}\right)$R30° phase. (a) fcc, (b) hcp, (c) alloy and (d) faulted alloy.

structures, yet not really in excellent agreement with the experimental $I(E)$ curves.

Next, the possibility of mixed surface geometry was tested by incoherently mixing the hcp and faulted alloy structures. This led to a significant improvement in the *R*-factor. The best agreement was gained with a 40:60 mix of hcp and faulted alloy structures, with Pendry *R*-factor of 0.26. The experimental and calculated $I(E)$ curves for the 40:60 mix of hcp and faulted alloy structures are shown in Fig. 4.

In an earlier study [9] the vertical distance between the Te and the first layer copper atoms was calculated to be 2.34 Å (bridge site). Our value for this parameter is 2.31 Å for hcp site, which agrees nicely with the earlier value. For faulted alloy structure the number is 0.88 Å, this difference can be explained by the different adsorption site. The Cu–Te bond length for the 0.33 ML coverage structure is about the same as in the case of the 0.08 ML coverage.

For the 0.33 ML layer coverage the level of agreement is moderate. The *R*-factor resolution is however better due to the larger data set. The data is also more evenly split between integer and fractional order spots. One complication in comparing the different models arises from the fact that they have different numbers of adjustable parameters. This occurs especially with the coexisting structures, which have additional free parameters compared to most other models. Clearly, more adjustable parameters allow a better fit, regardless of whether the underlying model is better or worse. In the case of $\left(2\sqrt{3}\times 2\sqrt{3}\right)$ structure the improvement in agreement gained by mixing the hcp and alloy structures is smaller than the Pendry variance, which clearly indicates that the better fit is due to larger number of free parameters compared to the other models. In the case of $\left(\sqrt{3}\times\sqrt{3}\right)$ structure however the improvement in *R*-factor is almost twice the Pendry variance and thus the mixed surface structure is an appealing option.

4.2. DFT

The same trial geometries as in the case of LEED were used to calculate the adsorption energies using DFT. Table 3 lists the adsorption energies for different trial geometries for both 0.08 ML and 0.33 ML coverages. For the sake of clarity the higher coverage structure is discussed first.

4.2.1. $\left(\sqrt{3}\times\sqrt{3}\right)R30°$ phase

At 0.33 ML coverage the alloy structure is slightly favored over the other possible geometries. Fig. 5 shows the local density of states (DOS) plots for the $\left(\sqrt{3}\times\sqrt{3}\right)$R30° structure. By comparing the p-DOS (Fig. 5a1 and a2) and d-DOS (Fig. 5b1 and b2), the right hand side of the p-DOS double peak can be attributed to the tellurium–tellurium interaction (because there is no clear interaction with the d-DOS of copper) and the left hand side can be attributed to tellurium–copper interaction. A 3-dimensional view of the partial charge density for the hcp structure is plotted in Fig. 6. The partial charge density that corresponds to the energy range of the Te–Te interaction peak in Fig. 5 is shown with violet and the partial charge density that corresponds to

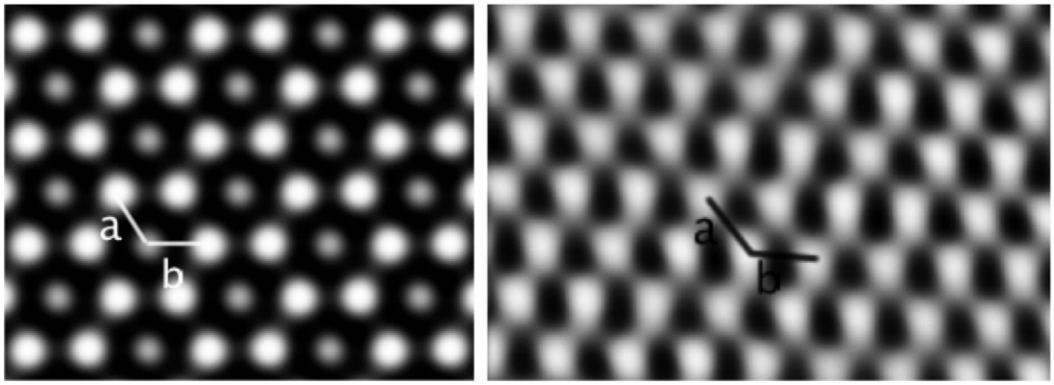

Fig. 8. On the left DFT simulated STM image for the alloy structure. On the right the measured STM image. The measurement parameters are current setpoint 1.7 nA, gap voltage 1.5 V, loop gain 2.4% and original scan size 10 nm × 10 nm. The experimental image has been Fourier filtered.

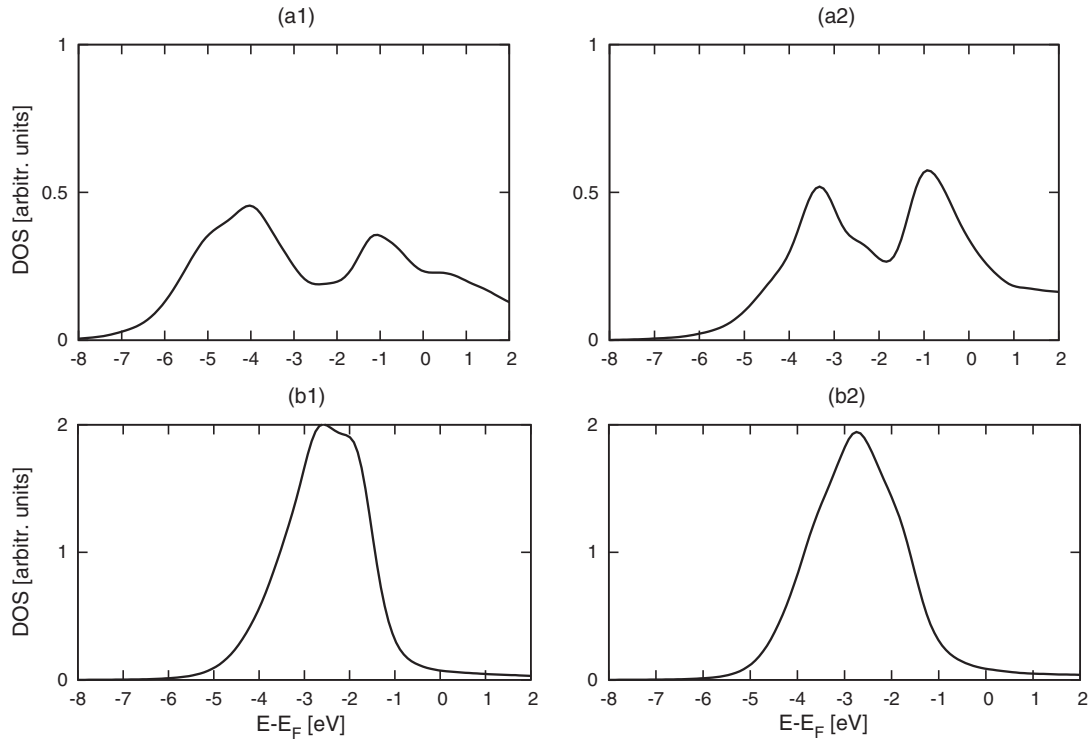

Fig. 9. The local DOS of the surface atoms of the $\left(2\sqrt{3}\times 2\sqrt{3}\right)$R30° phase. (a1) The p-DOS of Te at the surface alloy. (a2) The p-DOS of Te at the hcp site. (b1) The d-DOS of the Cu atom next to the surface alloy Te. (b2) The d-DOS of the Cu atom next to the Te on the hcp site.

the energy range of copper–tellurium peak is shown with yellow. This figure clearly demonstrates that the Te–Te interaction is antibonding and that the Te–Cu interaction is bonding. Fig. 5a1 and a2 show that the antibonding is stronger (peak is more pronounced) in the case of the hcp structure. The same goes also with the Te–Cu interaction, which in the hcp case is as important as the Te–Te interaction. In the alloy structure the Cu–Te interaction is stronger than the Te–Te interaction, which can be understood with the adsorption geometry; in the alloy structure the Te atoms sit deeper and thus don't 'see' each other as well as in the case of hcp, where the Te atoms sit above the surface layer. From Fig. 5 it is clear that the antibonding Te–Te interaction is the dominating interaction in the hcp case and in the case of alloy structure the Cu–Te interaction is dominating. Fig. 7 shows some simulated STM images calculated based on the DFT results. Fig. 8 compares experimental [11] and simulated STM images. The simulated image is for the alloy structure, which matches up well with the experimental image. The other simulated images do not give similar match with the experiment. For example, for the fcc (Fig. 7a) and hcp (Fig. 7b) adsorption, Te protrudes above the surface in the simulated images. However the experimental image does not show any protrusions. Also the symmetry of the simulated faulted alloy image (Fig. 7d) does not agree with the experimental image.

4.2.2. $\left(2\sqrt{3}\times 2\sqrt{3}\right)R30°$ phase

At 0.08 ML coverage the DFT calculations show no clear preference for any of the trial geometries used. The top site structure is energetically unstable but for hollow, bridge and alloy structures the adsorption energies are very similar. Fig. 9 shows the local DOS plots for the surface atoms in the $\left(2\sqrt{3}\times 2\sqrt{3}\right)$R30° structure. These plots look very similar compared to those in the higher coverage case. Now, when the coverage is lower and thus the Te atoms are further away from each other, the antibonding effect is weaker. The p-DOS of the alloy and hcp look more alike in this case than at higher coverage, which can also be seen in the adsorption energies which are now closer to each other for the hcp and the alloy. Fig. 10 shows some simulated STM images calculated based on the DFT results. All the DFT simulated images except the faulted alloy show triangular 'defect' type structure, which might originate from Moire fringes. In the experiment [11] these defects are not seen for $\left(2\sqrt{3}\times 2\sqrt{3}\right)$R30° phase. As noted above, the simulated images for the hcp and fcc adsorption sites have Te atoms "sitting" above the surface. This does not agree with the experimental image. The DFT simulated structures that have the least Moire structure are the two alloy structures, which are shown next to the experimental STM image in Fig. 11.

Table 3 shows that the adsorption energy increases with the decreasing coverage. This can be due to the fact that with the decreasing coverage, the Te atoms cease to interact with each other. The Te–Te distance in the $\left(\sqrt{3}\times\sqrt{3}\right)$ phase is 4.42 Å, which is very close to the nearest neighbor distance measured on the Te(0001) plane (4.46 Å), but in $\left(2\sqrt{3}\times 2\sqrt{3}\right)$-phase the Te–Te distance is 8.84 Å.

5. Discussion

This paper presents the Cu(111)-Te surface structure for two distinct coverages; 0.08 ML and 0.33 ML. At 0.08 ML coverage the adsorption energies from DFT are almost equal for hollow, bridge and the two alloy structures. However LEED results show that the hcp hollow and alloy structures are favored over other possible geometries, thus it is possible to say that the surface alloy formation has started at 0.08 ML coverage. This is in agreement with the earlier study where a binding energy shift of the Te $3d_{5/2}$ half peak was observed at the earliest coverage.

When the Te coverage increases to 0.33 ML, surface alloy formation becomes more prominent. At this coverage the DFT calculations show that the surface alloy is energetically favored over other structures. The LEED $I(E)$ results indicate that the alloying is not yet compete, suggesting that the structure is not an equilibrium one, and the best

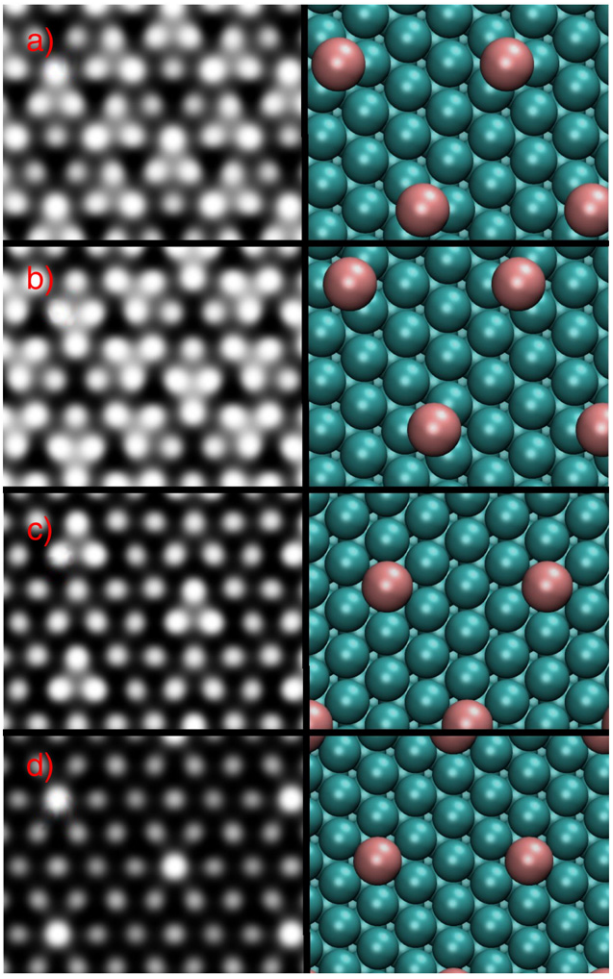

Fig. 10. Simulated STM images along with the top view of the structure for the hollow and alloy adsorption geometries in the $\left(2\sqrt{3}\times 2\sqrt{3}\right)$R30° phase. (a) fcc, (b) hcp, (c) alloy and (d) faulted alloy.

agreement is gained when a mixture of hcp-hollow and faulted alloy is introduced. The results of our LEED and DFT calculations indicate that as Te goes on the surface, it immediately starts going into the surface forming a normal unfaulted surface alloy. As coverage increases, the surface alloy "flips" to faulted surface alloy at about 0.33 ML. This reconstruction from normal alloy to faulted alloy is clear from the LEED results, but not so clear in the case of DFT, where the normal alloy is slightly favored over the faulted alloy. This kind of behavior has been earlier reported for Sb on Cu(111) surface [19,20]. The outermost surface contains both Cu and Te atoms in the hcp hollow sites, leading to a stacking fault at the alloy surface interface but the process is dynamical and with increasing coverage, a bulk alloy structure starts to form, but if this is not yet favorable, additional atoms go into hcp sites.

Acknowledgments

IMM, DH and MOK thank the EPSRC for studentship support. AC, ML and KP thank the Academy of Finland (#263634, #218186, #218546), CSC-IT Center for Science Ltd and FGI—Finnish Grid Infrastructure. The LEED calculations were performed using programs from the Barbieri/Van Hove Symmetrized Automated LEED package.

Appendix A. Supplementary data

Supplementary data to this article can be found online at http://dx.doi.org/10.1016/j.susc.2013.11.018.

References

[1] J. Zhou, X. Wu, A. Duda, G. Teeter, S.H. Demtsu, Thin Solid Films 515 (18) (2007) 7364.
[2] A.S. Pashinkin, L.M. Pavlova, Inorg. Mater. 41 (9) (2005) 939.
[3] A.S. Pashinkin, V.A. Fedorov, Inorg. Mater. 39 (6) (2003) 539.
[4] G. Teeter, Thin Solid Films 515 (2007) 7886.
[5] J. Zhou, X. Wu, A. Duda, G. Teeter, S.H. Demtsu, Thin Solid Films 515 (2007) 7364.
[6] K. Neyvasagam, N. Soundararajan, Ajaysoni, G.S. Okram, V. Ganesan, Phys. Status Solidi B 245 (2008) 77.
[7] B. Spath, K. Lakus-Wollny, J. Fritsche, C.S. Ferekides, A. Klein, W. Jaegermann, Thin Solid Films 515 (2007) 6172.
[8] G. Teeter, J. Appl. Phys. 102 (2007) 034504.
[9] S. Andersson, I. Marklund, J. Martinson, Surf. Sci. 12 (1968) 269.

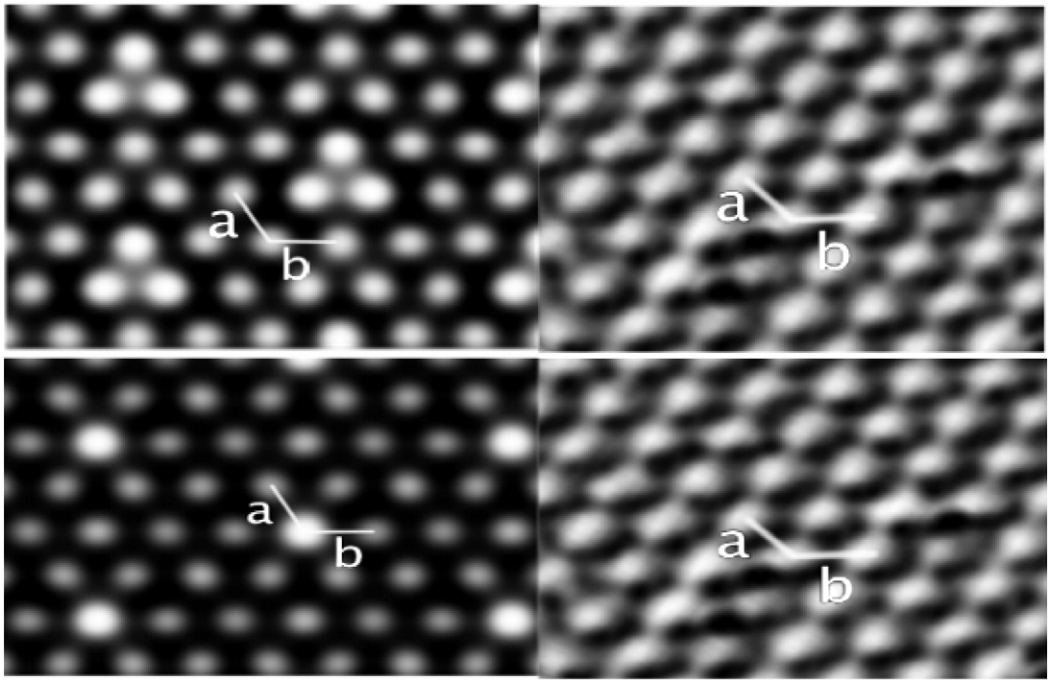

Fig. 11. On the left DFT simulated STM images for the alloy (top) and faulted alloy (bottom) structures. On the right the measured STM images. The measurement parameters are current setpoint 2 nA, gap voltage 2.3 V, loop gain 2% and original scan size 50 nm × 50 nm. The experimental image has been Fourier filtered and cropped.

[10] F. Comin, P.H. Citrin, P. Eisenberger, J.E. Rowe, Phys. Rev. B26 (1982) 7060.
[11] M.O. King, I.M. McLeod, D. Hesp, V.R. Dhanak, M. Kadodwala, D.A. MacLaren, Surf. Sci. 606 (2012) 1353.
[12] P. Samanta, W.N. Unertl, J. Vac. Sci. Technol. A 5 (1987) 568.
[13] P. Samanta, W.N. Unertl, Surf. Sci. 175 (1986) L721.
[14] T.W. Capehart, T.N. Rhodin, G.W. Graham, K. Jacobi, Phys. Rev. B 26 (1982) 7027.
[15] T.N. Rhodin, T.W. Capehart, Surf. Sci. 89 (1979) 337.
[16] T.W. Capehart, T.N. Rhodin, J. Vac. Sci. Technol. 16 (1979) 594.
[17] S. Nagashima, Appl. Surf. Sci. 145 (1999) 73.
[18] Norihito Ikemiya, Daisuke Iwai, Koji Yamada, Ruxandra Vidu, Shigeta Hara, Surf. Sci. 369 (13) (1996) 199208.
[19] S.A. de Vries, W.J. Huisman, P. Goedtkindt, M.J. Zwanenburg, S.L. Bennett, I.K. Robinson, E. Vlieg, Surf. Sci. 414 (1998) 159.
[20] P. Bailey, T.C.Q. Noakes, D.P. Woodruff, Surf. Sci. 426 (3) (1999) 358372.
[21] J.J. Yeh, Atomic Calculation of Photoionization Cross-Sections and Asymmetry Parameters, Gordon and Breach Science Publishers, Langhorne, PE (USA), 1993.
[22] J.J. Yeh, I. Lindau, At. Data Nucl. Data Tables 32 (1985) 1.
[23] L.C. Feldman, J.W. Mayer, Fundamentals of Surface and Thin Film Analysis, North-Holland, Amsterdam, 1986. 228.
[24] A. Barbieri, M.A. Van Hove, Private communication http://www.ap.cityu.edu.hk/personal-website/Van-Hove.htm.
[25] J.B. Pendry, J. Phys. C Solid State Phys. 13 (1980) 937.
[26] G. Kresse, J. Hafner, Phys. Rev. B 47 (1993) 558.
[27] G. Kresse, J. Hafner, J. Phys. Condens. Matter 6 (1994) 8245.
[28] G. Kresse, J. Hafner, Phys. Rev. B 49 (1994) 14251.
[29] G. Kresse, J. Furthmüller, Comput. Mater. Sci. 6 (1996) 15.
[30] G. Kresse, J. Furthmüller, Phys. Rev. B 54 (1996) 11169.
[31] P.E. Blöchl, Phys. Rev. B 50 (1994) 17953.
[32] J.P. Perdew, K. Burke, M. Ernzerhof, Phys. Rev. Lett. 77 (1996) 3865.
[33] H.J. Monkhorst, J.D. Pack, Phys. Rev. B 13 (1976) 5188.
[34] http://www.p4vasp.at/.
[35] G.E. Laramore, Phys. Rev. B 9 (1974) 12041215.
[36] H. Nowotny, Z. Metallkd. 37–38 (1946–47) 40.
[37] W. Braun, G. Held, Surf. Sci. 594 (13) (2005) 1.